Journal of the Australian Ceramic Society (2023) 59:105–115
https://doi.org/10.1007/s41779-022-00816-0

RESEARCH

Fabrication of nitride films by co-sputtering of high-entropy alloys and tungsten

Ding-Chiang Hu[1] · Dong-Hau Kuo[1] · Jin-Yih Kao[2] · Chun-Sheng Chen[2] · Chung-Chen Tsao[2] · Chun-Yao Hsu[2]

Received: 3 July 2022 / Revised: 8 August 2022 / Accepted: 11 September 2022 / Published online: 8 November 2022
© The Author(s) under exclusive licence to Australian Ceramic Society 2022

Abstract

This study produces (AlCrNbSiTiV-W)N films onto soda-lime glass and SUS 304 stainless steel substrates using reactive co-sputtering. The target materials are high-entropy alloys (HEAs, AlCrNbSiTiV, 2 inches in diameter) and tungsten (W, 3 inches in diameter). The deposition time is 15 min, the sputtering power for targets of W and (AlCrNbSiTiV) is 200 W, the substrate temperature is 150 °C and the properties of (AlCrNbSiTiV-W)N films for various $N_2/(Ar+N_2)$ flow ratios (0, 5, 10, 15, and 20%) are determined the mechanical properties (such as surface morphology, film hardness, wear, surface roughness, and corrosion resistance) and microstructure (such as grain size, lattice structure, and elemental content). The XRD results show that (AlCrNbSiTiV-W)N film has a W (110) diffraction peak at 2θ~40°. The microstructure of (AlCrNbSiTiV-W)N film is uniform, dense structure, and there is no peeling or cracking. As the $N_2/(Ar+N_2)$ flow ratio increases to 20%, the highest hardness is 37.52 GPa, Young's modulus is 210.4 GPa, the lowest friction coefficient is 0.516, and the best corrosion resistance is –221.6 mV.

Keywords Magnetron sputtering · High-entropy alloys · (AlCrNbSiTiV-W)N films · Analysis of mechanical properties

Introduction

Surface modification using electroplating [1], electroless coating [2], atomic layer deposition (ALD) [3], chemical vapor deposition (CVD) [4], or physical vapor deposition (PVD) [5] is the most effective method to increase the cost performance ratio for surface quality. PVD magnetron sputtering produces films with a dense structure and superior properties. Nitride films (such as TiN, ZrWN, CrWN, TiAlN, and TiCN) are transition metal films and have high hardness, good wear resistance, and excellent thermal resistance and chemical stability, so they are widely used in cutting tools, molds, and surface coatings for components to extend service life and reduce manufacturing costs. The formation of nitrides generally involves binary systems but multi-element (above binary) systems have been developed to meet the needs of various industrial applications. Multi-element nitrides feature better mechanical and physical properties than binary systems, so many studies focus on improving the properties of nitride multi-system thin films. A co-sputtering system uses more than two targets and allows parametric adjustment of a single substrate during the sputtering process. Co-sputtering is widely used in the optoelectronics, aerospace, biomedical, and semiconductor industries. High-entropy alloys (HEAs) are present in simple solid solutions, such as single face-centered cubic (FCC), body-centered cubic (BCC), or in the amorphous phase, so selecting an appropriate alloy solid solution composition can improve the mechanical properties of a film on a substrate, such as hardness, corrosion resistance, oxidation resistance, and wear resistance [6].

Ye et al. first proposed the concept of multi-element HEAs [7–12], and in subsequent studies [13–16] showed that the effect of multi-element HEAs involves four main effects: high-entropy effect, sluggish diffusion, severe lattice distortion, and the cocktail effect [9]. Yamamoto et al. [17, 18] proposed a process to coat a cutting tool using a five-element TiCrAlSiN system, which gives better cutting

✉ Chung-Chen Tsao
aetcc@mail.lhu.edu.tw

✉ Chun-Yao Hsu
cyhsu@mail.lhu.edu.tw

[1] Department of Materials Science and Engineering, National Taiwan University of Science and Technology, Taipei 10607, Taiwan

[2] Department of Mechanical Engineering, Lunghwa University of Science and Technology, Taoyuan 33306, Taiwan

properties than coating using a ternary or quaternary system. After 2 h of vacuum annealing at 1000 °C, the thin film still maintains its original hardness value. Hsieh et al. [19] determined the effect of different coating parameters on (AlCrNbSiTiV)N thin films using reactive magnetron sputtering. The results of this study show that the thin film structure is FCC (NaCl type), with high hardness and excellent oxidation resistance. The hardness depends on the residual internal stress, grain size, and film density. Lai et al. [20] determined the effect of nitrogen flow and nitrogen content on (AlCrTaTiZr)N thin films and showed that the microstructure and mechanical properties of (AlCrTaTiZr)N thin films are superior to those of conventional nitride hard coatings.

A traditional nano-layered pearlite structure significantly increases the strength and wear resistance of iron but is not suited to use in high temperatures. An et al. [21] developed the pearlite structure from the single main element iron alloy into a multi-principal element alloy (MPEA) using a eutectoid reaction, and used the thermal stability of MPEA to form strong pearlite. The high temperature wear resistance increases the strength and wear performance of MPEA at high temperatures. Chang et al. studied CBN cutting using direct current magnetron sputtering (DCMS) and high-power impulse magnetron sputtering (HIPIMS). The Grey-Taguchi experimental parameters (deposition time, substrate DC bias, DC power, and substrate temperature) were used to optimize the parameter settings for the deposition of (AlCrNbSiTiV)N thin films on tools and glass substrates [22]. The experimental results show that the (AlCrNbSiTiV)N thin film coating has enhanced performance characteristics and the coating film is uniform, dense, has a high hardness value, and adheres perfectly to the glass substrate. Pedersen et al. [23] used density functional theory (DFT) with supervised machine learning to predict the CO and H adsorption energies on all surface sites on the (111) surfaces of disordered CoCuGaNiZn and AgAuCuPdPt. The HEA composition was optimized by adding sites with weak hydrogen adsorption to inhibit the formation of molecular hydrogen and sites with strong CO adsorption to favor CO reduction. This produces a coating with high strength and good ductility that is suited to use in various industries. Safety, environment, and economic concerns mean that the development of high-performance alloys with high strength and high ductility is ongoing. Traditional strengthening mechanisms are becoming more effective, so ductility is decreased. Alloy design concepts for conventional alloys limit the development of new alloys with heterogeneous microstructures that feature good strength-plastic synergy. Sathiyamoorthi and Kim [24] made an exhaustive literature review of the strength-ductility synergy of HEAs with heterogeneous microstructures.

Experimental method and procedures

Experimental materials and pretreatment

This study uses DC reactive magnetron co-sputtering equipment to deposit (AlCrNbSiTiV-W)N thin films. The sputtering equipment includes a sputtering system and a vacuum system. A mechanical rotary pump is used to pump the cavity pressure to 6×10^{-2} torr and a cryo pump is used to create a cavity vacuum of less than 5.5×10^{-6} torr. The pressure control valve and the gas mass flow controller respectively stabilize the cavity pressure and regulate the nitrogen/argon gas mass flow ratio. Ar (purity 99.999%) is the working gas and N_2 (purity 99.995%) is the reaction gas. The targets that are used for magnetron sputtering are equimolar purity > 99.9% (AlCrNbSiTiV) (2 inches in diameter) and 99.95% purity W (3 inches in diameter), and the two targets are placed on the back. Above the plate, and the back plate, there are permanent magnets and the thin films are directly deposited onto soda-lime glass and SUS 304 stainless steel using a DC plasma generator to test the thin film material and abrasion quality.

Before sputtering in the vacuum chamber, the sample was shaken with deionized water in an ultrasonic shaker (deionized water) for 10 min to remove impurities on the surface of the test piece and was then shaken with isopropyl alcohol (isopropyl alcohol) in an ultrasonic shaker After 15 min, an oil stain on the surface of the test piece was removed. The test piece was then repeatedly cleaned with deionized water for 10 min to remove residual isopropanol. The substrate was blown dry with nitrogen gas and covered with vacuum heat-resistant tape on the glass test piece. After sputtering, the film thickness was measured by tearing it off.

Experimental process and parameter settings

A DC reactive magnetron sputtering system was used to produce (AlCrNbSiTiV-W)N thin films. The sputtering power for targets of W and (AlCrNbSiTiV) was 200 W, respectively. The working temperature was 150 °C and the deposition time was 15 min. However, the voltage required to start the discharge arc for targets of W and (AlCrNbSiTiV) is about 300–400 V. The effect of the various $N_2/(Ar + N_2)$ flow ratios (0, 5, 10, 15, and 20%) on the mechanical properties and microstructure of (AlCrNbSiTiV-W)N thin films was determined. The sputtering parameters for the (AlCrNbSiTiV-W)N thin film for this study are shown in Table 1.

Analysis of film microstructure and properties

A field emission electron microscope (FESEM, JSM, JEOL 6500) was used to observe the cross-section and surface

Table 1 Deposition parameters for (AlCrNbSiTiV-W)N thin film

Deposition parameters	Specification	
Target	AlCrNbSiTiV (2 inches in diameter)	W (3 inches in diameter)
Substrate	Soda-lime glass, SUS 304 stainless steel	
Base pressure (torr)	5×10^{-6}	
Substrate to target distance (mm)	60	
Working pressure (torr)	5.5×10^{-3}	
Substrate temperature (°C)	150	
Substrate rotate vertical axis (rpm)	50	
Substrate DC bias (V)	0	
Gas	Ar, N_2	
(Ar + N_2) total flow (sccm)	20	
Deposition time (min)	15	
DC power (watt)	200	
Function of N_2/(Ar + N_2) flow ratio = 0, 5, 10, 15, and 20%		

morphology of the thin films and EDS was used to determine the elemental content of the thin films. X-ray diffraction (PANalytical-X'Pert PRO MPD) used an incident light source of Cu Kα at a wavelength of 0.15418 nm, the scanning range was 20 ~ 80° and the scanning rate was 5°/min to measure the grain size and microstrain for the thin film. A dynamic microhardness tester (Fischer HM-2000) that uses a diamond indentation head to apply a force of 30 mN on the thin film was used. The thin film hardness value (GPa) and the load and displacement curve use data for a duration of 30 s. A Vickers tester (Mitutoyo HM-113) with a load of 50gf was used for 10 s and the size of the indentation was measured.

The Oliver-Pharr method [25] was used to calculate the elastic modulus of the thin film from the load and displacement curve. A ball-on-disk abrasion tester (CSM Ball-on-disk Tribometer) was used to grind the ball with Al_2O_3. The ball P roughness is 0.08 µm, the diameter is 6 mm, the hardness is 788 HV, the wear trajectory is a circle with a diameter of 10 mm, a distance of 30 m, tangential speed of 10 cm/s, a load of 1 N, an ambient temperature of 27 °C, and a humidity of 65%. This was used to measure the friction coefficient of the thin film. A surface profiler (Kosaka Instruments, SEF-3500DK31) and a probe (model PU-DJ2S) were used to measure the surface roughness of the thin film by the centerline average roughness method (R_a).

To measure corrosion, samples were maintained at room temperature. After exposure to corrosive 3.5% NaCl solution for 30 min, a three-electrode setup was used to determine the effect for various N_2/(Ar + N_2) flow ratios using an open circuit potential (OCP) and potentiodynamic polarization scan. The flow rate, the Taffer curve for the (AlCrNbSiTiV-W)N thin film, the corrosion potential (Ecorr), and corrosion current density (Icorr) are determined.

Results and discussion

This study uses DC reactive co-sputtering to produce (AlCrNbSiTiV-W)N thin films on soda-lime glass and SUS 304 stainless steel substrates using various N_2/(Ar + N_2) flow ratios (0, 5, 10, 15, and 20%), using AlCrNbSiTiV alloys and W metal targets. The effect of the N_2/(Ar + N_2) flow ratio on the mechanical properties and microstructure of (AlCrNbSiTiV-W)N thin films is determined.

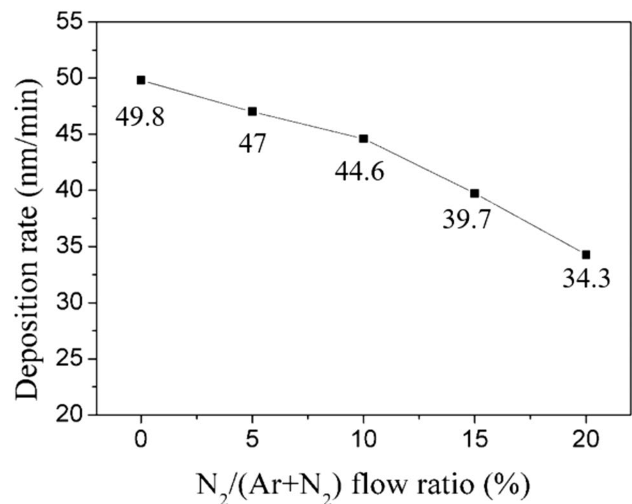

Fig. 1 Correlation between deposition rates and N_2/(Ar + N_2) flow ratios

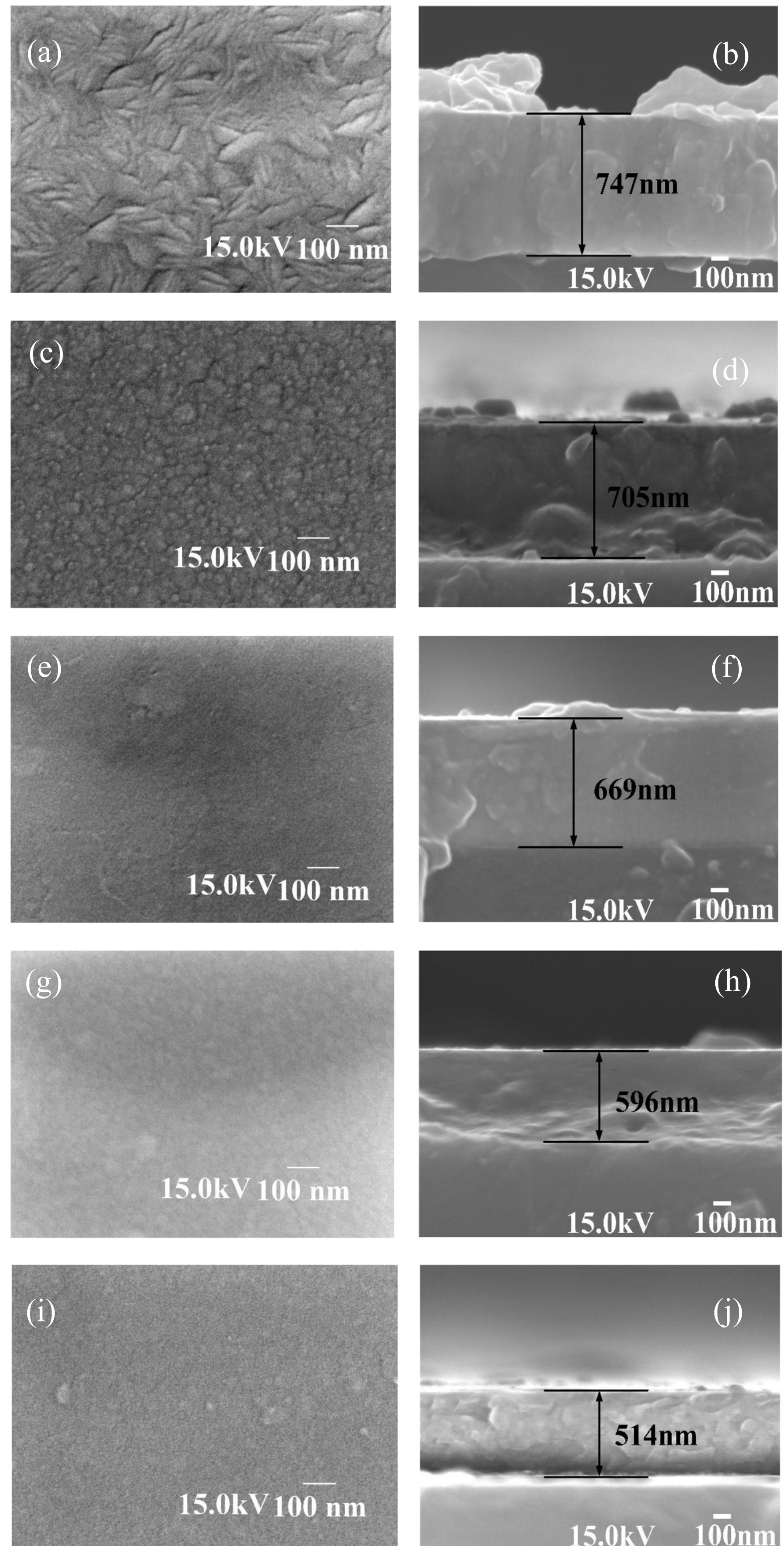

Fig. 2 SEM image of surface and cross-sectional morphologies of (AlCrNbSiTiV-W)N thin films that are deposited using various $N_2/(Ar+N_2)$ flow ratios: (**a**, **b**) 0%, (**c**, **d**) 5%, (**e**, **f**) 10%, (**g**, **h**) 15% and (**i**, **j**) 20%

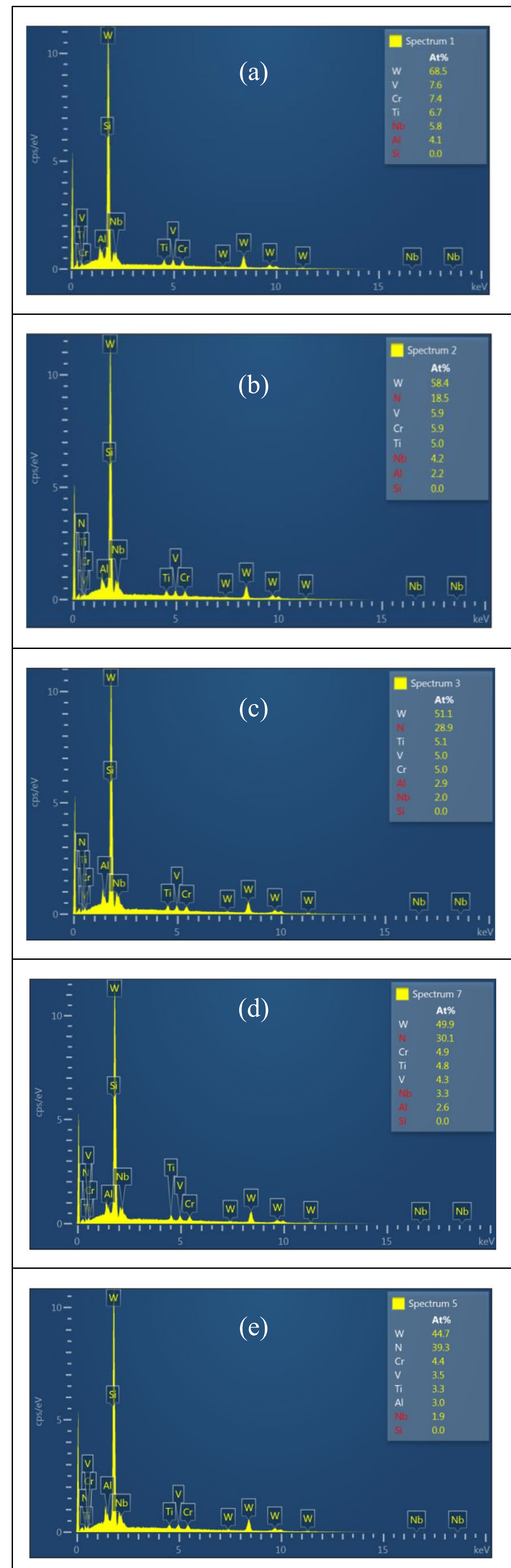

Fig. 3 EDS spectra for (AlCrNbSiTiV-W)N thin films that are produced using various $N_2/(Ar+N_2)$ flow ratios: (**a**) 0%, (**b**) 5%, (**c**) 10%, (**d**) 15%, and (**e**) 20%

Morphology and microstructure of (AlCrNbSiTiV-W)N

Figure 1 shows the deposition rates for (AlCrNbSiTiV-W)N thin films for various $N_2/(Ar+N_2)$ flow ratios. Figure 1 shows that if the $N_2/(Ar+N_2)$ flow ratio increases, the deposition rate decreases significantly (the change is about 31.1%). If the N_2 flow rate increases, the (AlCrNbSiTiV-W)N thin film deposition structure is incomplete and the deposition rate decreases. A previous study [26] showed that if the target, the substrate, and different nitrogen ratios undergo surface reaction, increasing the nitrogen ratio causes the surface of the target to react with nitrogen to produce nitrides, which is called the target poisoning effect (or target poisoning) [27–30]. This retards sputtering, and the thin film that is deposited is not so thick. Figure 2 shows that the surface of the (AlCrNbSiTiV-W)N thin film features uniform particle nucleation and a consistent grain size, and no obvious hole defects are observed under SEM magnification, so the thin film has a stable microstructure. If (AlCrNbSiTiV-W)N thin films are deposited using various $N_2/(Ar+N_2)$ flow ratios (0 ~ 20%), the deposited film decreases in thickness from 747 to 514 nm, due to the target poisoning effect.

The EDS results for the compositions of (AlCrNbSiTiV-W)N thin films that are produced using various $N_2/(Ar+N_2)$ flow ratios are shown in Fig. 3. The W component accounts for the largest proportion. Since the diameter of the W target is larger than that of the (AlCrNbSiTiV) target, the W target is more likely to sputter out more W atoms than (AlCrNbSiTiV) target. The relationship between on concentration of specific elements and the $N_2/(Ar+N_2)$ flow ratios is shown in Fig. 4. As the N_2 flow rate increases, the N component ratio increases from 0 to 39.3 at. % and the W component ratio decreases from 68.5 to 44.7 at. %. The component ratios for other elements (AlCrNbSiTiV) is slightly decreased. There is a high Si content in the (AlCrNbSiTiV) target but the EDS analysis shows no Si main peak, possibly because the signals for Si (Si-Kα signal is 1.741 keV) and W (W-Mα signal is 1.775 keV) are too close and the EDS beam energy is too low, so the detection signals overlap.

Figure 5 shows signal overlap, which often occurs in the semiconductor industry due to the presence of refractory materials (such as tungsten metal diffusion layers) on the wafer. A high-energy beam (wavelength dispersion spectroscopy, WDS) is then used for analysis. Matysiak et al. [31] also noted a similar signal overlap for the analysis of Haynes 282® superalloy. The resolution for the elemental for EDS is also at least 0.1 ~ 0.5 wt. %, but the resolution for WDS is at least 200 ~ 1000 ppm [27].

XRD results

Figure 6 shows the XRD spectrum analysis for (AlCrNbSiTiV-W)N thin films. For a $N_2/(Ar+N_2)$ flow ratio of 20%, W changes from a single main peak [110] to W_2N [111], [200], [220], and [311]. The [220] result for W_2N produces a thin film structure but other elements are not identified in the XRD results because the content is too low. The as-prepared (AlCrNbSiTiV-W)N thin film samples can also affect the scattering of other metal phases due to severe lattice deformation. The crystalline properties of (AlCrNbSiTiV-W)N thin films for various $N_2/(Ar+N_2)$ flow ratios are shown in Table 2. The microstrain for the grain structure is calculated as follows: ($\varepsilon = \beta\cos\theta/4$) (Chopra). The respective microstrain for the various $N_2/(Ar+N_2)$ flow ratios is 0.028, 0.041, 0.155, 0.192, and 0.642 m/m. The results show that increasing $N_2/(Ar+N_2)$ flow ratio not only leads to a decrease in grain size, but also an increase in plane distance and microstrain. When the $N_2/(Ar+N_2)$ ratio is lower than 6.7%, the amorphous structure of the coating has a higher electronegativity compared to other constituent elements such as Cr, Al, Nb, Si, and V. It is negative and occupies the center of the short-range order [32] and reduces the free volume [33], which not only reduces the element volume, but also deepens the interatomic potential wall. The addition of nitrogen atoms to the amorphous coating increases the elastic modulus. When the $N_2/(Ar+N_2)$ ratio is higher than 20%, the formation of nitrides is the main reason for the sudden increase in elastic modulus (plane distance) [34]. The formation of long-range ordered atomic structures improves the packing efficiency of atoms, resulting in higher elastic modulus values. The Hall-Patch Eq. (1) shows that the smaller the grain size, the greater is the microstrain [35].

$$\sigma_y = \sigma_0 + \kappa_y/\sqrt{D} \quad (1)$$

σ_y is the yield strength
σ_0 is the lattice strength against dislocation displacement

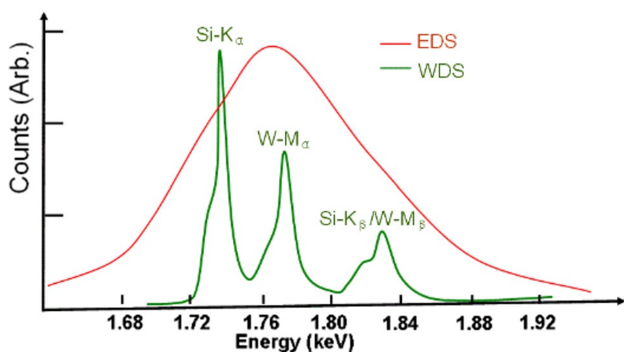

Fig. 5 Signal overlap phenomena for the EDS and WDS analyses

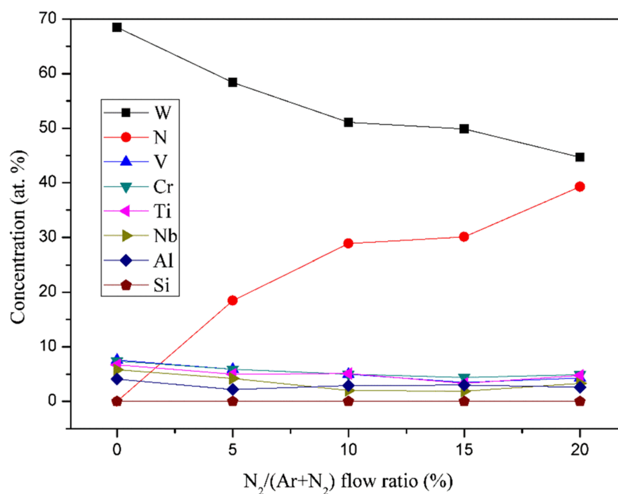

Fig. 4 Visual representation of EDS results for (AlCrNbSiTiV-W)N thin films

κ_y is the enhancement coefficient
D is the grain size

Hardness and elastic recovery values

For a dynamic microhardness measurement, to measure the hardness of (AlCrNbSiTiV-W)N thin films prepared that are produced using various $N_2/(Ar+N_2)$ flow ratios, the indentation depth is defined as one-tenth of the film thickness, in order to avoid touching the substrate. There is often springback, which is more representative of the correct hardness value of the thin film. The greater the indentation load,

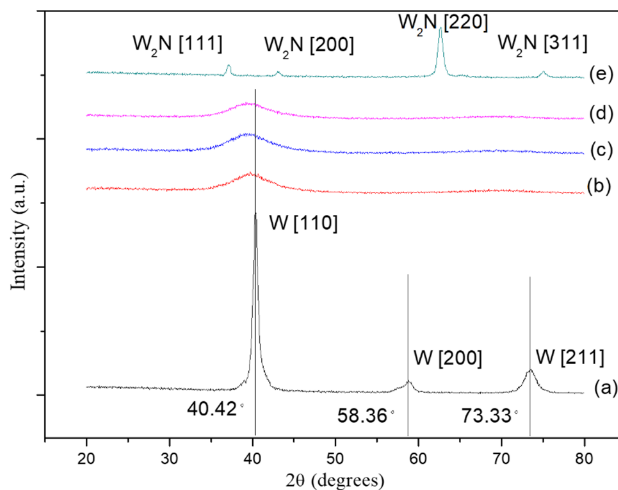

Fig. 6 XRD diffraction peaks for (AlCrNbSiTiV-W)N thin films that are produced using various $N_2/(Ar+N_2)$ flow ratios: (**a**) 0%, (**b**) 5%, (**c**) 10%, (**d**) 15%, and (**e**) 20%

Table 2 Crystalline properties of (AlCrNbSiTiV-W)N thin films that are produced using various $N_2/(Ar+N_2)$ flow ratios

$N_2/(Ar+N_2)$ (%)	W main peak [110] 2θ (°)	Full width at half maximum β (rad)	Grain size D (nm)	Plane distance d_{hkl} (nm)	Microstrain ε (m/m)
0	40.33	0.492	17.215	0.2235	0.028
5	40.22	0.590	15.763	0.2225	0.041
10	39.64	0.629	13.436	0.2272	0.155
15	38.84	0.960	8.781	0.2317	0.192
20	37.23	1.181	7.103	0.2413	0.292

Table 3 Hardness properties of (AlCrNbSiTiV-W)N thin films that are produced using various $N_2/(Ar+N_2)$ flow ratios

$N_2/(Ar+N_2)$ (%)	Hardness (GPa/HV)	Young's modulus E (GPa)	H/E ratio	H^3/E^2 ratio	h_r (nm)	h_{max} (nm)	R_e (%)
0	17.88/608.8	135.4	0.13	0.311	74.57	195.52	61.86
5	19.07/643.1	137.2	0.12	0.281	79.95	185.33	56.86
10	26.64/655.2	168	0.16	0.669	49.96	172.89	71.10
15	27.32/669.5	161.4	0.17	0.782	53.06	170.22	68.83
20	37.52/682.3	210.4	0.18	1.193	32.70	149.27	78.09

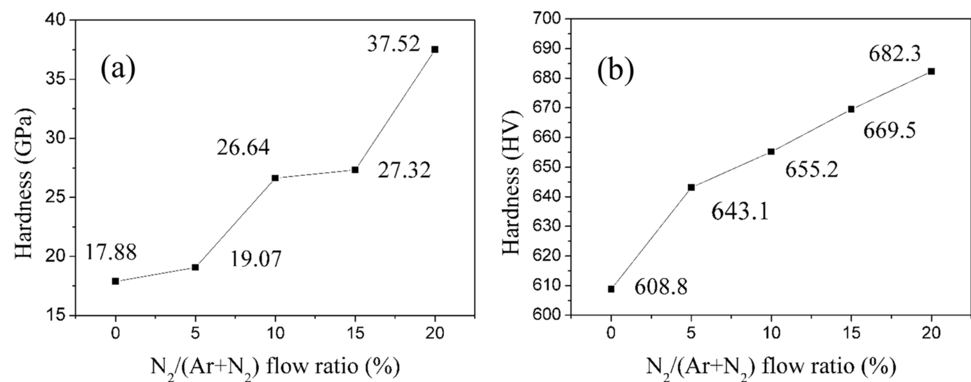

Fig. 7 Hardness values for (AlCrNbSiTiV-W)N thin films that are produced using various $N_2/(Ar+N_2)$ flow ratios: (**a**) GPa and (**b**) HV

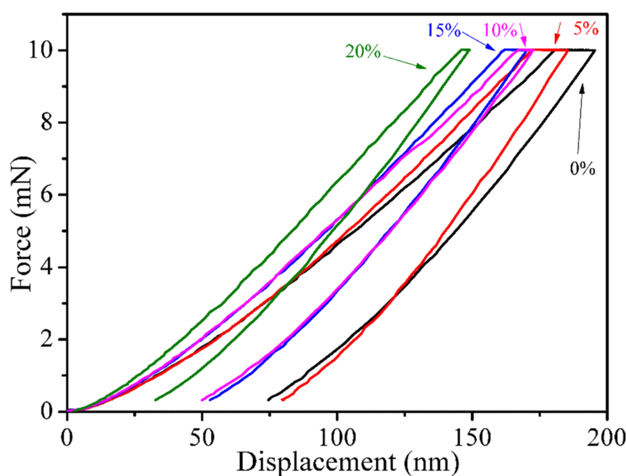

Fig. 8 Nano-indentation force and displacement diagram for (AlCrNbSiTiV-W)N thin films that are produced using various $N_2/(Ar+N_2)$ flow ratios

the greater is the film hardness. The maximum loading for (AlCrNbSiTiV-W)N thin films that are produced using various $N_2/(Ar+N_2)$ flow ratios is about 10.00 mN and the maximum loading indentation depth (h_{max}), residual depth (h_r), elastic recovery amount (R_e), and hardness (H), are shown in Table 3. The R_e is calculated as: $(h_{max}-h)/h_{max} \times 100\%$.

Figure 7 shows the hardness values (GPa/HV) for (AlCrNbSiTiV-W)N thin films that are produced using various $N_2/(Ar+N_2)$ flow ratios. Figure 7 and Table 3 show a $N_2/(Ar+N_2)$ flow ratio of 20% produces the greatest hardness (37.52GPa) and the greatest value for elastic recovery (78.09%). Tung et al. [36] found that when the $N_2/(Ar+N_2)$ ratio was increased to 20%, the increased hardness of the high-entropy nitride coating was attributed to more compressive residual stress and an increase in the nitrogen concentration in the coating. And this compressive residual stress is mainly from point defects. Moreover, during the sputtering process, atoms on the surface of the two targets (AlCrNbSiTiV and W) are excited by the plasma, so the pressure near the two targets is much greater than the pressure outside the

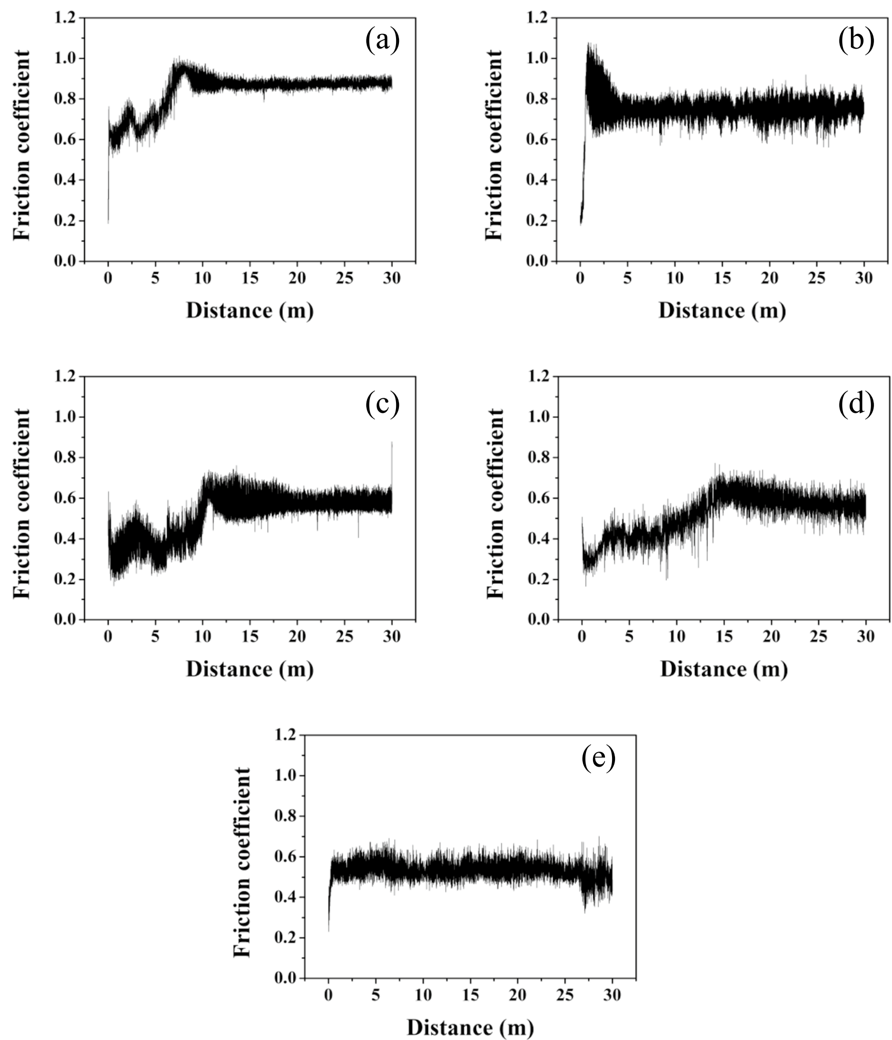

Fig. 9 Relationship between friction coefficient and wear distance for (AlCrNbSiTiV-W)N thin films that are produced using various $N_2/(Ar+N_2)$ flow ratios: (**a**) 0%, (**b**) 5%, (**c**) 10%, (**d**) 15%, and (**e**) 20%

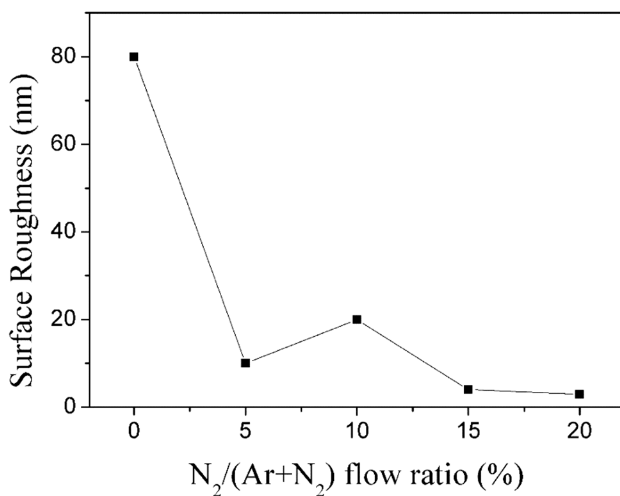

Fig. 10 Surface roughness of (AlCrNbSiTiV-W)N thin films that are produced using various $N_2/(Ar+N_2)$ flow ratios

substrate. The vapor flow from the atoms on the surface of the two targets far exceeds the flow of $N_2/(Ar+N_2)$. The flow rate for atomic vapor on the surface of the two targets is also much greater than the flow of $N_2/(Ar+N_2)$, so nitrogen does not enter the surface of the substrate. The pressure above the substrate surface is also lower than the pressure at the two

Table 4 Relationship between grain size and surface roughness for (AlCrNbSiTiV-W)N thin films that are produced using various $N_2/(Ar+N_2)$ flow ratios

$N_2/(Ar+N_2)$ (%)	Grain size (nm)	Surface roughness, R_a (nm)
0	17.215	80
5	15.763	10
10	13.436	20
15	8.781	4
20	7.170	3

Table 5 Calculated electrochemical properties of (AlCrNbSiTiV-W)N thin films that are produced using various $N_2/(Ar+N_2)$ flow ratios

$N_2/(Ar+N_2)$ (%)	βa (mV)	βc (mV)	B (mV)	R_p (μΩ/cm^2)	Corrosion potential (mV)	Corrosion current (μAmp/cm^2)
0	52.3	24.8	7.31	3.28	−443.8	2.232
5	24.9	28.2	5.79	3.37	−421.1	1.707
10	23.3	14.3	3.85	2.93	−226.9	1.314
15	7.8	25.1	2.59	2.84	−223.1	0.911
20	7.1	8.8	1.71	2.15	−211.6	0.793

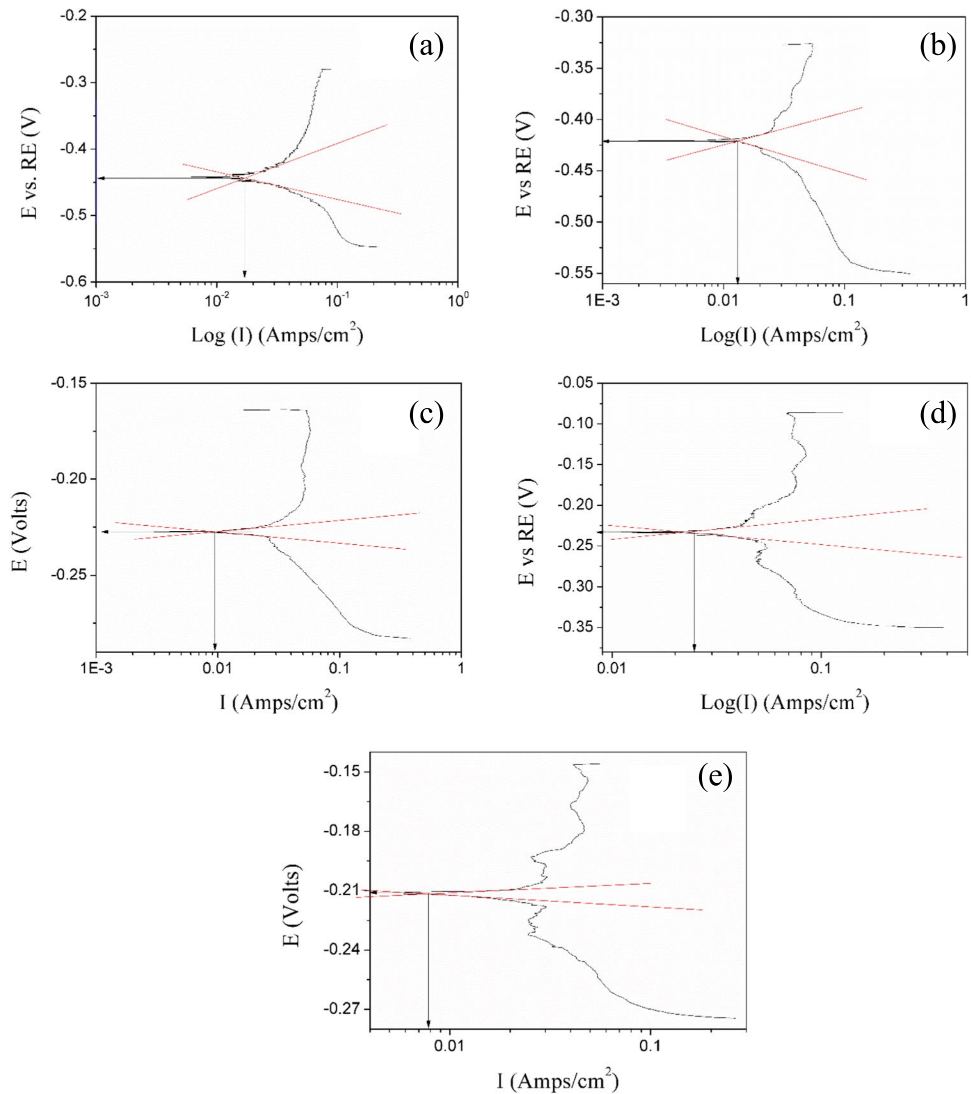

Fig. 11 Actual polarization plots for (AlCrNbSiTiV-W)N thin films that are produced using various $N_2/(Ar+N_2)$ flow ratios: (**a**) 0%, (**b**) 5%, (**c**) 10%, (**d**) 15%, and (**e**) 20%

targets. The dissolution of nitrogen in the cavity involves three stages: (1) nitrogen molecules move towards the substrate, (2) diatomic nitrogen molecules are absorbed by the surface of the substrate and dissociated into monoatomic nitrogen, and (3) N atoms pass through the surface layer of the substrate and diffuse deep into the interior. Therefore, as the $N_2/(Ar+N_2)$ flow ratio increases, the hardness of the substrate surface increases.

A previous study [26] shows that the highest hardness value for W_2N is 24 GPa, which is in good agreement with the hardness results for this study. Figure 8 shows the load and displacement curves for (AlCrNbSiTiV-W)N thin films that are produced using various $N_2/(Ar+N_2)$ flow ratios. Figure 8 shows that Young's modulus (E) for (AlCrNbSiTiV-W)N thin films that are produced using various $N_2/(Ar+N_2)$ flow ratios is 135.4, 157.2, 168.0, 161.4, and 210.4 GPa,

respectively. The hardness value is used to calculate the *H*/*E* and H^3/E^2 ratios. The greater the *H*/*E* ratio, the more resistant is the film to abrasion. The larger the H^3/E^2 ratio, the greater is the film's resistance to plastic deformation [28]. Table 3 shows that a $N_2/(Ar+N_2)$ flow ratio of 20% produces the highest values for *H*/*E* (0.18) and H^3/E^2 (1.193). A $N_2/(Ar+N_2)$ flow ratio of 20% produces a thin film with the best wear resistance and the greatest resistance to plastic deformation.

Wear test

A ball-to-disk abrasion tester was used to grind Al_2O_3 balls with a roughness of 0.08 µm, a diameter of 6 mm, and a hardness of 788 HV. The diameter of the abrasion track is 10 mm, the distance is 30 m, the tangential speed is 10 cm/s, the load is 1 N and the temperature was 27 °C and humidity was 65%. The coefficient of friction for various $N_2/(Ar+N_2)$ flow ratios for (AlCrNbSiTiV-W)N thin films were measured. The results in Fig. 9 show that the friction coefficient for (AlCrNbSiTiV-W)N thin films that are produced using various $N_2/(Ar+N_2)$ flow ratios is about 0.833, 0.748, 0.521, 0.516, and 0.531, respectively. A greater N_2 content gives a lower friction coefficient and a shorter distance is required to reach a steady state.

Surface roughness

The surface roughness of (AlCrNbSiTiV-W)N thin films that are produced using various $N_2/(Ar+N_2)$ flow ratios was measured using a surface profiler with a scratch length of 3 mm, as shown in Fig. 10. The results in Fig. 10 and Table 4 show that as the $N_2/(Ar+N_2)$ flow ratio increases, the grain size decreases, so there is a decrease in surface roughness, which is related to hardness.

Analysis of resistance to corrosion

Table 5 shows the electrochemical properties of (AlCrNb-SiTiV-W)N thin films that are produced using various $N_2/(Ar+N_2)$ flow ratios. The corrosion resistance potential increases as the $N_2/(Ar+N_2)$ flow ratio increases. A $N_2/(Ar+N_2)$ flow ratio of 20% produces the best corrosion resistance, as shown in Fig. 11. N_2 has excellent electronegative properties, so it attracts more electrons and it combines easily with W to form W_2N, which is a non-metallic compound with high hardness. A $N_2/(Ar+N_2)$ flow ratio of 20% generates more W_2N, so corrosion resistance is increased.

Conclusion

This study uses a DC reactive magnetron co-sputtering system with AlCrNbSiTiV and tungsten targets to sputter the (AlCrNbSiTiV-W)N thin films, a fixed sputtering power (200 W) and chamber temperature (150 °C), and various $N_2/(Ar+N_2)$ flow ratios and soda-lime glass and SUS 304 substrates. The results of this study are summarized as follows:

1. As the $N_2/(Ar+N_2)$ flow ratio increases, the deposition rate of (AlCrNbSiTiV-W)N thin films decreases. There are too many reactive gases in the environment, so the target material is poisoned. Therefore, during the reactive sputtering process, the deposition rate of the target material is reduced and the deposition time is prolonged.
2. The SEM observation and XRD calculations show that as the $N_2/(Ar+N_2)$ flow ratio increases, the grain size of the (AlCrNbSiTiV-W)N thin film decreases and the mechanical properties (hardness, Young's) of the (AlCrNbSiTiV-W)N thin film are improved. These include the Young's modulus, wear resistance, and corrosion resistance. Roughness is reduced.
3. The EDS analysis shows that as the $N_2/(Ar+N_2)$ flow ratio increases, the N content and W content in the thin film change linearly.
4. The optimal $N_2/(Ar+N_2)$ flow ratio for a sputtered (AlCrNbSiTiV-W)N thin film is 20%. This ratio gives the smallest grain size (7 nm) and the highest N content in the nitride film (39 nm). The highest hardness is (37.52 GPa/682 HV), the highest wear resistance is ($H/E=0.18$, $H^3/E^2=1.193$, friction coefficient = 0.531), the lowest surface roughness (R_a) is 3 nm and corrosion resistance is good (E_{corr}: −221.6 mV/I_{corr}: 0.793 µAmp/cm^2). However, this ratio gives the lowest deposition rate is 34.37 nm/min and the highest structural microstrain is 0.642 m/m.

Funding The authors gratefully acknowledge the support of the Ministry of Science and Technology of the Republic of China, through Grant nos. MOST 110–2622-E-262–001, MOST 111–2622-E-262–001 and MOST 111–2221-E-262–005.

Declarations

Conflict of interest The authors declare no competing interests.

References

1. Sheveiko, O., Kazakevich, A., Straumal, B., Vershinin, N., Startsev, D.: Modification of metal surface by electroplating and vacuum arc deposition, pp. 5513–5520. Frontiers in Corrosion. Science and Technology, Granada, Spain (2002)
2. Zhao, W., Wang, Z., Qiao, L., Liu, S. and Zhao, H., Photocatalytic surface modification og PI film for electroless copper plating, Advances in Condensed Matter Physics, Article ID 1619581 (2018).
3. Kemell, M., Farm, E., Ritala, M., Leskela, M.: Surface modification of thermoplastics by atomic layer deposition of Al_2O_3 and TiO_2 thin films. Eur. Polymer J. **44**, 3564–3570 (2008)

4. Yang, R., Asatekin, A., Gleason, K.H.: Design of conformal, substrate-independent surface modification for controlled protein adsorption by chemical vapor deposition (CVD). Soft Matter **8**, 31–43 (2012)
5. Hendry, J.A., Pilliar, R.M.: The fretting corrosion resistance of PVD surface-modified orthopedic implant alloys. J. Biomed. Mater. Res. **58**, 156–166 (2001)
6. Gao, M.C., Jablonski, P.D., Hawk, J.A. and Alman, D.E., High-entropy alloys: formation and properties, ASME 2018 Symposium on Elevated Temperature Application of Materials for Fossil, Nuclear, and Petrochemical Industries, Seattle, WA, USA (2018).
7. Tsai, M.H., Yeh, J.W.: High entropy alloys: a critical review. Material Research Letters **2**, 107–123 (2014)
8. Yeh, J.W., Chen, S.K., Lin, S.J., Gan, J.Y., Chin, T.S., Shun, T.T., Tsau, C.H., Chang, S.Y.: Nanostructured high-entropy alloys with multiple principal elements: novel alloy design concepts and outcomes. Adv. Eng. Mater. **6**, 299–303 (2004)
9. Chen, T.K., Shun, T.T., Yeh, J.W., Wong, M.S.: Nanostructured nitride films of multi-element high-entropy alloys by reactive DC sputtering. Surf. Coat. Technol. **188–189**, 193–200 (2004)
10. Tong, C.J., Chen, Y.L., Yeh, J.W., Lin, S.J., Chen, S.K., Shun, T.T., Tsau, C.H., Chang, S.Y.: Microstructure characterization of $Al_xCoCrCuFeNi$ high-entropy alloy system with multiprincipal elements. Metall. and Mater. Trans. A. **36**, 881–893 (2005)
11. Tong, C.J., Chen, M.R., Yeh, J.W., Lin, S.J., Chen, S.K., Shun, T.T., Chang, S.Y.: Mechanical performance of the $Al_xCoCrCuFeNi$ high-entropy alloy system with multiprincipal elements. Metall. and Mater. Trans. A. **36**, 1263–1271 (2005)
12. Wu, J.M., Lin, S.J., Yeh, J.W., Chen, S.K., Huang, Y.S., Chen, H.C.: Adhesive wear behavior of $Al_xCoCrCuFeNi$ high-entropy alloys as a function of aluminum content. Wear **261**, 513–519 (2006)
13. Yeh, J.W., Recent progress in high-entropy alloys, Annales de Chimie – Science des Materiaux 31, pp. 633–648 (2006).
14. Tsai, M.H., Yeh, J.W., Gan, J.Y.: Diffusion barrier properties of AlMoNbSiTaTiVZr high-entropy alloy layer between copper and silicon. Thin Solid Films **516**, 5527–5530 (2008)
15. Shen, H., Zhang, J., Hu, J., Zhang, J., Mao, Y., Xiao, H., Zhou, X., Zu, X.: A novel TiZrHfMoNb high-entropy alloy for solar thermal energy storage. Nanomaterials **9**, 248 (2019)
16. Kim, H.W., Kim, N.H.: Preparation of GaN films on ZnO buffer layers by rf magnetron sputtering. Appl. Surf. Sci. **236**, 192–197 (2004)
17. Yamamoto, K., Kujime, S., Takahara, K.: Structural and mechanical property of Si incorporated (Ti, Cr, Al)N coatings deposited by arc ion plating process. Surf. Coat. Technol. **200**, 1383–1390 (2005)
18. Ezura, H., Ichijo, K., Hasegawa, H., Yamamoto, K., Hotta, A., Suzuki, T.: Microhardness, microstructurd and thermal stability of (Ti, Cr, Al, Si)N films deposited by cathodic arc method. Vacuum **82**, 476–481 (2008)
19. Hsieh, T.H., Hsu, C.H., Wu, C.Y., Kao, J.Y., Hsu, C.Y.: Effects of deposition parameters on the structure and mechanical properties of high-enropy alloy nitride films. Curr. Appl. Phys. **18**, 512–518 (2018)
20. Lai, C.H., Lin, S.J., Yeh, J.W., Chang, S.Y.: Preparation and characterization of AlCrTaTiZr multielement nitride coatings. Surf. Coat. Technol. **201**, 3275–3280 (2006)
21. An, X.L., Liu, Z.D., Zhang, L.T., Zou, Y., Xu, X.J., Chu, C.L., Wei, W., Sun, W.W.: A new strong pearlitic multi-principal element alloy to withstand wear at elevated temperatures. Acta Mater. **227**, 117700 (2022)
22. Chang, K.S., Chen, K.T., Hsu, C.Y., Hong, P.D.: Growth (AlCrNbSiTiV)N thin films on the interrupted turning and properties using DCMS and HIPIMS system. Appl. Surf. Sci. **440**, 1–7 (2018)
23. Pedersen, J.K., Batchelor, T.A.A., Bagger, A., Rossmeisl, J.: High-entropy alloys as catalysts for the CO_2 and CO reduction reactions. ACS Catal. **10**, 2169–2176 (2020)
24. Sathiyamoorthi, P., Kim, H.S.: High-entropy alloys with heterogeneous microstructure: processing and mechanical properties. Prog. Mater Sci. **123**, 100709 (2022)
25. Ma, D., Chung, W.O., Liu, J., He, J.: Determination of Young's modulus by nanoindentation. Sci. China Ser. E: Technol. Sci. **47**, 398–408 (2004)
26. Lou, B.S., Yang, Y.C., Qiu, Y.X., Diyatmika, W., Lee, J.W.: Hybrid high power impulse and radio frequency magnetron sputtering system for TiCrSiN thin film depositions: Plasma characteristics and film properties. Surf. Coat. Technol. **350**, 762–772 (2018)
27. Depla, D., De Gryse, R.: Target poisoning during reactive magnetron sputtering: Part I: the influence of ion implantation. Surf. Coat. Technol. **183**, 184–189 (2004)
28. Wang, N., Wang, Z., Aust, K., Erb, U.: Effect of grain size on mechanical properties of nanocrystalline materials. Acta Metall. Mater. **43**, 519–528 (1995)
29. Depla, D., De Gryse, R.: Target poisoning during reactive magnetron sputtering: Part II: the influence of chemisorption and gettering. Surf. Coat. Technol. **183**, 190–195 (2004)
30. Guttler, D., Abendroth, B., Grotzschel, R., Moller, W.: Mechanisms of target poisoning during magnetron sputtering as investigated by real-time in situ analyses and collisional computer simulation. Appl. Phys. Lett. **85**, 6134 (2004)
31. Matysiak, H., Zagorka, M., Andersson, J., Nalkowiec, A., Cygan, R., Rasinki, M., Pisarek, M., Andrzejezuk, M., Kubiak, K., Kurzydlowski, K.J.: Microstructure of Haynes ® 282® superalloy after vacuum induction melting and investment casting of thin-walled components. Materials **6**, 5016–5037 (2013)
32. Sheng, H.W., Luo, W.K., Alamgir, F.M., Bai, J.M., Ma, E.: Atomic packing and short-to-medium-range order in metallic glasses. Nature **439**, 419–425 (2006)
33. Yiu, P., Diyatmika, W., Bonninghoff, N., Lu, Y.C., Lai, B.Z., Chu, J.P.: Thin film metallic glasses: properties, applications and future. J. Appl. Phys. **127**, 030901 (2020)
34. Lin, Y.C., Hsu, S.Y., Lai, Y.T., Kuo, P.H., Tsai, S.Y. and Duh, J.G., Effect of the $N_2/(Ar+N_2)$ ratio on mechanical properties of high entropy nitride $(Cr_{0.35}Al_{0.25}Nb_{0.12}Si_{0.08}V_{0.20})Nx$ films**,** Materials Chemistry and Physics **274,** 125195 **(2021).**
35. Mostafapor, A., Mohammadinia, V.: Mechanical properties and microstructure evolution of AA1100 aluminum sheet processed by accumulative press bonding process. Acta Metall. Sin. **29**, 735–741 (2016)
36. Tung, H.M., Huang, J.H., Tsai, D.G., Ai, C.F., Yu, G.P.: Hardness and residual stress in nanocrystalline ZrN films: effect of bias voltage and heat treatment. Mater. Sci. Eng., A **500**, 104–108 (2009)

Publisher's note Springer Nature remains neutral with regard to jurisdictional claims in published maps and institutional affiliations.

Springer Nature or its licensor (e.g. a society or other partner) holds exclusive rights to this article under a publishing agreement with the author(s) or other rightsholder(s); author self-archiving of the accepted manuscript version of this article is solely governed by the terms of such publishing agreement and applicable law.